

# High-speed range and velocity measurement using frequency scanning interferometry with adaptive delay lines [Invited]

CHRISTOS A. PALLIKARAKIS,\*  JONATHAN M. HUNTLEY,  AND PABLO D. RUIZ

Loughborough University, Wolfson School of Mechanical, Electrical and Manufacturing Engineering, Loughborough LE11 3TU, UK

\*Corresponding author: C.A.Pallikarakis@lboro.ac.uk

Received 28 July 2020; revised 7 September 2020; accepted 8 September 2020; posted 10 September 2020 (Doc. ID 403858); published 27 October 2020

Range (i.e., absolute distance), displacement, and velocity of a moving target have been measured with a frequency scanning interferometer that incorporates a 100,000 scan  $s^{-1}$  vertical-cavity surface-emitting laser with 100 nm tuning range. An adaptive delay line in the reference beam, consisting of a chain of switchable exponentially growing optical delays, reduced modulation frequencies to sub-gigahertz levels. Range, displacement, and velocity were determined from the phase of the interference signal; fine alignment and linearization of the scans were achieved from the interferogram of an independent reference interferometer. Sub-nanometer displacement resolution, sub-100-nm range resolution, and velocity resolution of 12  $\mu m s^{-1}$  have been demonstrated over a depth measurement range of 300 mm.

Published by The Optical Society under the terms of the [Creative Commons Attribution 4.0 License](https://creativecommons.org/licenses/by/4.0/). Further distribution of this work must maintain attribution to the author(s) and the published article's title, journal citation, and DOI.

<https://doi.org/10.1364/JOSAA.403858>

## 1. INTRODUCTION

A variety of pointwise optical techniques have been developed over the years for measurement of distance to a remote target. These include time of flight, phase shifting interferometry, and frequency scanning interferometry (FSI), also known as frequency-modulated continuous-wave (FMCW) lidar [1,2].

FSI is widely regarded as one of the most accurate methods when absolute distance, rather than changes in distance over time, is required. At its simplest, a tunable laser illuminates the target while undergoing a frequency scan at a constant rate. The target range is determined from the modulation frequency of the interference signal, produced when the back-reflected or back-scattered object wave is mixed with a reference wave from the same laser. The drawback of the method in its basic form is that the deduced range is dependent on the tuning rate of the laser, which can drift over time. The use of a separate reference interferometer avoids such errors: target range is determined as a multiple of the reference interferometer length through the ratio of modulation frequencies from the measurement and reference interferometers [3,4]. The inclusion of a gas absorption cell enables the calibration of the reference interferometer length traceable to international standards [5]. As calibration can be performed once per frequency scan, stability requirements of the reference interferometer are relaxed significantly with this approach.

Although the accuracy of FSI can be in the range of 1 part in  $10^6$  to 1 in  $10^8$ , it has long been recognized that the technique's "Achilles' heel," for highly accurate range measurement in practical industrial environments, is motion of the target, or changes in refractive index of the air, that occur during a scan. The error in the calculated range is equal to the intra-scan target displacement (or the effective displacement in the case of refractive index changes), multiplied by an amplification factor ( $\omega_c / \Delta\omega$ ), where  $\omega_c$  is the angular frequency of the emitted light at the center of the scan, and  $\Delta\omega$  is the angular frequency tuning range of the laser [3–7]. Several approaches to solving this problem have been proposed, such as the use of two lasers scanning simultaneously in opposite directions or at different rates [5–7], the generation of a frequency scan rate of opposite sign using four-wave mixing [8], the use of a laser with successive up–down frequency ramps [9], and the addition of a separate laser Doppler velocimeter (LDV) that informs the FSI system of the required error correction due to target motion [10].

When phase or frequency data are acquired from systems with frequency ramps of opposite sign, the average of the two values largely cancels the displacement error, while the difference between them provides a measure of the displacement or velocity, respectively, of the target. The ability to measure both range and velocity is attractive, but the cost and complexity

of many of the proposed systems is an obstacle to widespread industrial adoption.

New tunable laser (TL) sources with dramatic increases in scan repetition rate,  $f_s$ , have been developed in recent years, particularly within the optical coherence tomography (OCT) community. These are an interesting proposition for absolute distance measurement, not only for the increased coordinate acquisition rate, but also because the range error due to target motion scales inversely with  $f_s$ . Sources with large scan ranges  $\Delta\lambda$  of 100 nm or more about a center wavelength  $\lambda_c$  in the 1–1.5  $\mu\text{m}$  range are now available, with  $f_s$  values of upwards of  $10^5 \text{ s}^{-1}$  for vertical-cavity surface-emitting lasers (VCSEL) sources and  $10^6 \text{ s}^{-1}$  for Fourier-domain mode-locked lasers [11]. The first applications of such sources to medium scale ( $\sim 0.75 \text{ m}$ ) ranging applications have been described recently [12].

High-speed sources have an inherent drawback, however, which is the resulting very high frequencies of the interference signal. In Ref. [12], a high-speed oscilloscope with 16 GHz bandwidth and  $50 \text{ GS s}^{-1}$  sampling rate was used as the data acquisition (DAQ) hardware. The cost of DAQs currently rises very dramatically above bandwidths of about 1 GHz. A solution to this problem is the adaptive delay line (ADL) concept, proposed in [13], which is a chain of  $N$  switches and  $N$  optical delays that follow an exponential sequence. Through an appropriate selection of switch positions, the modulation frequency can be reduced by a factor of  $2^N$ .

In the current paper, we describe the first combination of a high-speed VCSEL source running at  $10^5 \text{ scans s}^{-1}$ , with an ADL, to measure the range, displacement, and velocity of a target undergoing controlled vibration. Section 2 provides the background theory of FSI and ADLs. The experimental setup and numerical analysis of the interference signals are described in Sections 3 and 4, respectively, with results and discussion presented in Sections 5 and 6, before some concluding remarks in Section 7.

## 2. FREQUENCY SCANNING INTERFEROMETRY WITH ADAPTIVE DELAY LINES

### A. Frequency Scanning Interferometry

An FSI system requires a tunable light source. Within a single scan, the angular frequency of the light emitted by the source,  $\omega_e$ , should ideally vary linearly with time,  $t$ . In practice, however, there may be non-linear contributions, and, in general,  $\omega_e$  can be written as a Taylor series expansion as follows:

$$\omega_e = \omega_0 + \dot{\omega}_0 t + \frac{1}{2} \ddot{\omega}_0 t^2 + \dots, \quad (1)$$

where  $\omega_0$ ,  $\dot{\omega}_0$ , and  $\ddot{\omega}_0$  are the zeroth, first, and second time derivatives of  $\omega_e$  at the start of the scan ( $t = 0$ ).  $\dot{\omega}_0$  is the linear tuning rate, and  $\frac{1}{2} \ddot{\omega}_0 t^2$  represents the first non-linear term.

Light from the source is divided into object and reference beams; the object beam is reflected off the target, which may in general be moving, and subsequently interferes with the reference wave. The intensity of the resulting interference signal may be written as

$$I(t) = I_0 + I_1 \cos(\phi), \quad (2)$$

where  $I_0$  and  $I_1$ , the background (“dc”) intensity, and modulation envelope, respectively, are slowly varying functions of time, and  $\phi$  is the phase offset between the object and reference waves. A rigorous second-order analysis of the phase term, including a relativistic description of the Doppler shift from the moving target, is given by Reichold in [14] and results in the following expression:

$$\phi = \omega_e \frac{\Lambda}{c} + \left( \frac{\Lambda}{c} \right)^2 \left[ -\frac{\ddot{\omega}_0}{2} t + \frac{\dot{\omega}_0}{2} + \frac{\ddot{\omega}_0}{6} \frac{\Lambda}{c} \right]. \quad (3)$$

Here,  $\Lambda$  represents the optical path difference (OPD) between the object and reference waves, which is time-varying due to the motion of the target mirror (TM), and  $c$  is the speed of light. As pointed out by Reichold, the terms in the square brackets can be neglected in many situations, in comparison to the first term on the right-hand side of Eq. (3), and this is the case for the parameter values in the current experimental setup. For the remainder of the paper, we therefore make the approximation

$$\phi = \omega_e \frac{\Lambda}{c}. \quad (4)$$

Although  $\omega_e(t)$  may not be well-characterized, the phase changes  $\Delta\phi_M$  and  $\Delta\phi_R$  that occur over the course of a scan in the measurement and reference interferometers, with OPDs  $\Lambda_M$  and  $\Lambda_R$ , respectively, are related through Eq. (4) as follows:

$$\Lambda_M = \frac{\Delta\phi_M}{\Delta\phi_R} \Lambda_R. \quad (5)$$

$\Lambda_R$  is assumed to be constant through the scan, with its value determined by some independent means such as a gas absorption cell, frequency comb, or a frequency stabilized interferometer, as is done later in this paper. If  $\Lambda_M$  changes by  $\Delta\Lambda_M$  during the course of the scan, then the value calculated by Eq. (5) is in error by  $\Delta\Lambda_M \omega_e / \Delta\omega$ , as noted in the previous section.

The case of a traditional interferometer with a monochromatic source of wavelength  $\lambda_0$  can be derived from Eq. (4) by substituting  $\omega_e(t) = 2\pi c / \lambda_0$ , and  $\Lambda = \Lambda_0 - 2u_z$ .  $u_z$  is the displacement component of the mirror along the optical axis, in a direction towards the interferometer, during the course of the “scan,” and  $\Lambda_0$  is the initial OPD. This results in the following well-known equation for an out-of-plane interferometer:

$$u_z = -\frac{\lambda_0 \Delta\phi}{4\pi}. \quad (6)$$

A key parameter in an FSI system is the maximum modulation frequency of the interference signal,  $f$ , since this determines the bandwidth and sampling rate of the DAQ.  $f$  can be calculated from Eqs. (1) and (4) if we neglect non-linear terms for simplicity and take  $\dot{\omega}_0 = \Delta\omega / \Delta t$ , where  $\Delta t$  is the scan duration, which gives the result

$$f = \frac{1}{2\pi} \frac{d\phi}{dt} = \frac{1}{2\pi} \frac{\Delta\omega}{\Delta t} \frac{\Lambda}{c} \approx \Lambda f_s \frac{\Delta\lambda}{\lambda_c^2}. \quad (7)$$

$f_s = 1/\Delta t$  is the scan repetition rate,  $\lambda_c$  is the center wavelength, and the approximation in terms of wavelengths, which is valid for short scans, allows for easy evaluation of  $f$  from the

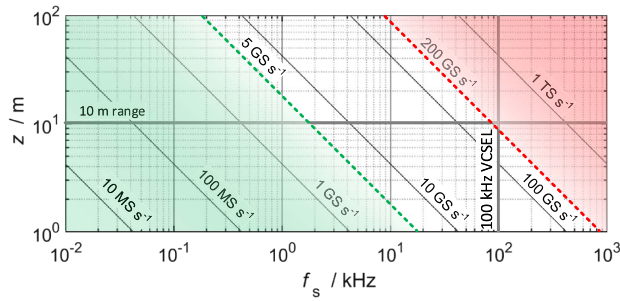


**Fig. 1.** Minimum DAQ sampling rates for a target at a range  $z$  and a laser with (saw-tooth) scan repetition rate  $f_s$ .

laser manufacturers' datasheets. Equation (7) is valid for saw-tooth waveforms; a pre-factor of 2 appears on the right-hand side for triangular waveforms, and  $\pi$  for sinusoidal waveforms. The dependence of  $f$  on  $f_s$  and on the target range  $z = \Lambda/2$ , predicted by Eq. (7) for the case of  $\lambda_c = 1300$  nm and  $\Delta\lambda = 100$  nm, is shown as a contour map in Fig. 1. All of the points on a given contour have identical bandwidth and sampling rate demands on the DAQ. The minimum sampling rate here is taken to be  $2f$ , as given by the Shannon sampling theorem. The green zone indicates the parameter space accessible by reasonably low-cost DAQs (below  $\sim \$1000$  per channel). The cost of DAQ hardware increases dramatically with sampling rate, and the red zone indicates the requirement for DAQ hardware that costs upwards of several  $\$100,000$  per channel. This is the regime that a VCSEL source with  $f_s = 100$  kHz runs into at a range of a few meters (m). In addition to the cost of the DAQs, the computational effort to process the  $>100$  GS $^{-1}$  data streams is too high, by at least 1–2 orders of magnitude, for real-time analysis by current reasonably priced graphics processing unit (GPU) or field-programmable gate array (FPGA) hardware. It was for these reasons that ADLs were developed, as summarized in the next sub-section.

## B. Adaptive Delay Lines

The concept of the ADL was first introduced in [13] and is outlined below. The ADL is a module placed in an interferometer's reference beam, as shown in Fig. 2(a) for the case of a Mach-Zehnder interferometer (MZI). In this example, a circulator is used to direct the object beam onto the target and to collect the back-reflected light. The interference signal between the object and reference beams is then measured by an auto-balanced pair of photodetectors and recorded by a DAQ board.

The ADL module consists of a chain of  $N$  switches, each of which selects one of two possible optical paths to the next switch. The OPD between the two paths from switch  $j$  will be denoted as  $\Lambda_j$ . The path differences are selected according to the following equation:

$$\Lambda_j = 2^j d_0, \quad j = 0, 1, \dots, N-1, \quad (8)$$

where  $d_0$  is the minimum OPD. An example is given in Fig. 2(b) for the case  $N = 3$ . Curved paths are shown since an ADL could be implemented using optical fibers or waveguides on a photonic integrated circuit (PIC). A recent example of a FMCW lidar, implemented on a silicon platform, is described in [15].

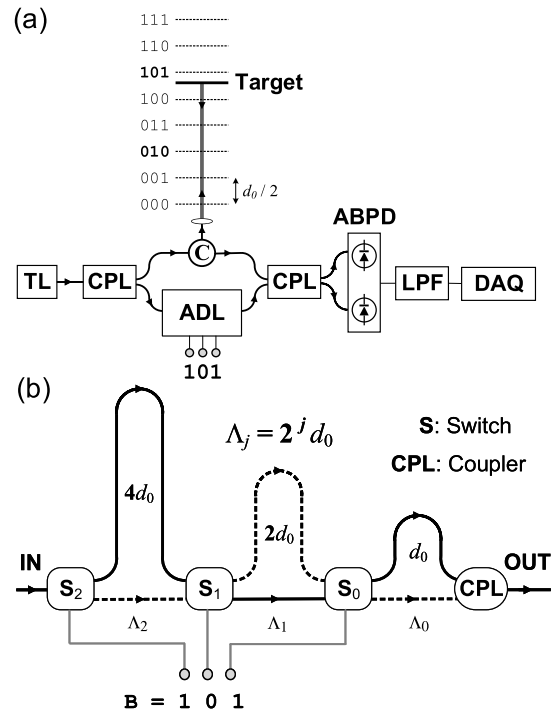


**Fig. 2.** Adaptive delay line (ADL) concept. (a) FSI system with ADL showing tunable laser (TL), couplers (CPL), circulator (C), auto-balanced photodetectors (ABPD), low-pass filter (LPF), and data acquisition board (DAQ). (b) Example of 3-bit ADL: continuous lines indicate the routing of the reference beam selected by switches  $S_0 \dots S_2$ , for bit configuration 101.

The state of switch  $j$  is defined by a binary digit  $b_j$ , where the value of one indicates that the longer path is selected, and a value of zero is the shorter path. The state of the ADL is completely specified by the bit pattern (byte)  $B = b_{N-1}b_{N-2} \dots b_1b_0$ . This controls, in turn, the location of the surface within the measurement volume, where the path difference between object and reference waves equals zero. Cross sections through the “zero-OPD surfaces” for the 3-bit example of Fig. 2(b) are shown as dotted lines in Fig. 2(a). These are spaced with a separation of  $d_0/2$  in the case of coaxial illumination and observation directions.

The benefits of the ADL were discussed in [13]. In general, for a given DAQ bandwidth and sampling rate, each additional switch in the chain doubles either the maximum range or the coordinate acquisition rate. Moreover, the restriction on the source coherence length ( $l_c \geq 2^N d_0$ ), which ultimately limits measurement range, is relaxed by a factor  $2^N$  to  $l_c \geq d_0$ .

## 3. EXPERIMENTAL

The optical setup used to demonstrate the ADL proof-of-principle [13] was modified slightly to allow combined range and displacement/velocity measurements, as shown in Fig. 3. Its design will be summarized here for completeness.

The ADL is a 3-bit device, the switching for which is carried out by manual rotation of achromatic half-wave plates (HWP) in front of polarizing beam splitters (PBS). If horizontally polarized light is incident on a given HWP, the beam passes through

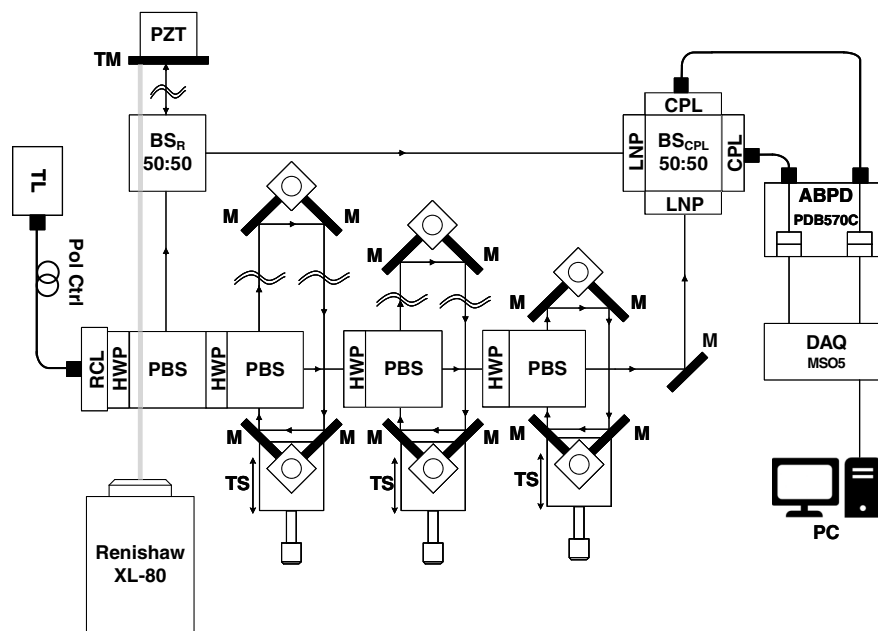


**Fig. 3.** Experimental optical setup, incorporating 3-bit ADL, to measure range and displacement.

the PBS to the next switch. Rotating the HWP by  $45^\circ$  causes vertically polarized light to enter the PBS. The beam is then directed around an optical delay loop consisting of two pairs of gold mirrors (M-M), where translation stages (TS) can be used to make fine adjustments of the delay lengths. The delays took the values  $d_0 \sim 240$  mm,  $d_1 \sim 490$  mm, and  $d_2 \sim 830$  mm. An additional HWP and PBS before the ADL are used as a variable ratio beam splitter (BS).

The TL source is a VCSEL (Thorlabs SL131090) that runs at a scan repetition rate of  $f_s = 100$  kHz, with a center wavelength of  $\lambda_c = 1300$  nm, and mode-hop-free tuning range of  $\Delta\lambda = 100$  nm. In its standard form, the laser produces linear frequency up-scans with very short down-scans. The use of up- and down-scanning lasers in the literature to separate velocity and range information has been described in Section 1. The laser was therefore customized by the manufacturer to produce up- and down-scans having a similar maximum tuning rate in both directions, though at the expense of an increase in signal modulation frequency by approximately  $2\times$  and some degradation of scan linearity. Ultimately only the frequency down-scan data was used in the experiments described in this paper.

Light is delivered to the interferometer through a single-mode, polarization-maintaining (SM PM) fiber and, after collimation with a reflective collimator (RCL), is split into the reference and object beams. Two linear polarizers (LNP) at the final  $BS_{CPL}$  ensure that the polarization states of object and reference waves are matched; the resulting interference signal is transmitted to an auto-balanced photodetector (ABPD) by a pair of SM PM fibers using couplers with achromatic doublets.

The target gold mirror (TM) that reflects the object beam was mounted on a piezoelectric (PZT) transducer (Burleigh Instruments PZ-81 linear translator, driven by a Burleigh R6-93 ramp generator). The PZT was in turn mounted on a rail assembly (not shown here), which allowed manual movement of the TM over a range of approximately 1 m and a corresponding

round trip range of  $\sim 2$  m. The position was monitored independently by means of a frequency stabilized interferometer (Renishaw XL-80). This is unable to measure absolute distance, as it operates at a fixed wavelength, but it can track changes in position (i.e., displacement) to an accuracy of  $0.5 \mu\text{m m}^{-1}$  and was used for calibration of the system.

The laser's 100 kHz repetition rate and 100 nm scan range mean that TM locations more than about 13 mm from a zero-OPD surface result in a modulation frequency,  $f$ , lying outside the 300 MHz bandwidth of the ABPDs. The experiment involved positioning the TM at a series of six fixed locations close to the zero-OPD surfaces for each of two ADL bit configurations (the 010 and 101). The location index and measured range with the Renishaw interferometer,  $z_{TM}$ , for the 12 locations, are shown in Table 1. The maximum modulation frequency was approximately 250 MHz for locations 1, 6, 7, and 12; 150 MHz for locations 2, 5, 8, and 11; and 50 MHz for locations 3, 4, 9, and 10.

At each location, a triangular waveform with a period of 25 ms was applied to the PZT, which resulted in a highly linear axial motion of the TM with peak-to-peak displacement of approximately  $1.0 \mu\text{m}$ . The PZT motion was characterized by recording the interference signal produced by a fixed-wavelength laser (Santec TSL-510,  $\lambda = 1270$  nm) in place of the TL. The PZT drive signal and interferometer signal are shown in Figs. 4(a) and 4(b), respectively, for one complete cycle of the PZT. The PZT motion was then extracted by separately fitting a five-parameter model to the PZT up-scan and down-scan intensity arrays [16]. The model allows for a quadratic (two-parameter) PZT response to the applied voltage; the non-linear contribution to the displacement was however very small for this particular PZT. The other three parameters were the dc intensity, the intensity modulation amplitude, and the initial phase offset between the object and reference arms of

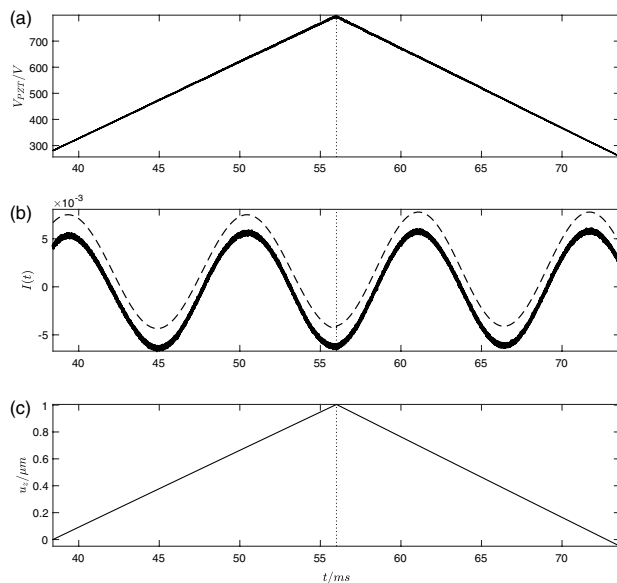


**Table 1. Measurement Interferometer Mean Frequency ( $\bar{A}$ ), Target Range ( $z_{TM}$ ), Standard Deviation in Range ( $\sigma_z$ ), and Displacement ( $\sigma_{u_z}$ ) for Each of 12 Target Mirror Locations****Bit Configuration: 010**

Location	1	2	3	4	5	6
$\bar{A}/\text{rad}$	-1.904420	-1.133434	-0.370212	0.392925	1.137153	1.908432
$z_{TM}/\text{mm}$	0.0001	2.6969	5.3675	8.0363	10.6398	13.3367
$\sigma_z/\text{nm}$	98.5	59.1	24.0	23.3	60.8	103.1
$\sigma_{u_z}/\text{nm}$	1.13	0.80	0.53	0.93	0.56	0.98

**Bit Configuration: 101**

Location	7	8	9	10	11	12
$\bar{A}/\text{rad}$	-1.941426	-1.123770	-0.382342	0.402078	1.155373	1.894744
$z_{TM}/\text{mm}$	297.3573	300.2164	302.8101	305.5547	308.1910	310.7758
$\sigma_z/\text{nm}$	98.6	52.7	18.0	19.8	53.2	92.4
$\sigma_{u_z}/\text{nm}$	1.01	0.92	0.58	0.74	0.89	0.89

**Fig. 4.** (a) PZT drive voltage over one complete cycle of the triangular wave. (b) Measured intensity signal (continuous line) and modeled intensity (dashed line, with small vertical shift for clarity) from fixed-wavelength laser. (c) Axial displacement of TM corresponding to model intensity in (b).

the interferometer. The modeled intensity, and corresponding underlying displacement of TM, are shown in Figs. 4(b) and 4(c).

For the experiments with the TL, the PZT drive signal was used to trigger a storage oscilloscope (Tektronix MSO54, 500 MHz,  $6.25 \text{ GS s}^{-1}$ , maximum record length: 62.5 Mpts) at a point in the waveform such that the maximum axial displacement occurred in the center of each dataset. The APBD signal was digitized on one channel of the storage oscilloscope. A second channel recorded the output of a reference interferometer (termed “ $k$ -clock” in the OCT community) contained within the laser control unit. This is a MZI with an optical delay of nominal value of 44 mm and produces a peak modulation frequency of around 890 MHz on the frequency up-scan and a little lower on the down-scan. A third channel recorded the

output signal from a fiber Bragg grating (FBG), which is, again, incorporated within the laser control box. This produces a pulse whenever the laser wavelength passes through the center wavelength, 1310 nm, of the FBG. Finally, the fourth channel recorded the output from the PZT control unit. The captured data sequences from all four channels, which were recorded synchronously, were then transferred to a personal computer (PC) for subsequent processing. The experimental data for all 12 locations are available from Ref. [17].

#### 4. NUMERICAL ANALYSIS

The recorded intensity from the measurement interferometer,  $I_M(t)$ , during a single 10  $\mu\text{s}$  duration up-down frequency scan is shown in Fig. 5(a), together with the FBG timing pulses. Each scan consists of approximately 32,000 sample points per channel, and, in total, 1000 up-down scans were recorded per dataset. The time-varying modulation frequency for the measurement and reference interferometers are represented by the spectrograms in Figs. 5(b) and 5(c), in which a sliding window length of 1000 sample points with 95% overlap was used.

Three distinct signal processing steps were developed to calculate range and displacement data from such a scan, as discussed in the following three sub-sections.

##### A. Signal Segmentation and Coarse Alignment

In order to measure displacement information from the phase changes of  $I_M(t)$ , it is necessary to segment the entire signal into individual frequency scans, similar to that shown in Fig. 5(a), and then to shift them along the time axis so as to align them with respect to one another. As the sampling rate will not normally be an integer multiple of  $f_s$ , alignment to sub-sample point accuracy is in general required.

The approach adopted here was to use the reference interferometer signal,  $I_R(t)$ , which is recorded in tandem with  $I_M(t)$ , as a stable “ruler” against which the shifts in  $I_M(t)$  due to displacement of the target could be measured. The reference interferometer fringe maxima can be thought of as the ruler markings and are separated by a constant wavenumber difference; however, as they are not labelled, a robust method

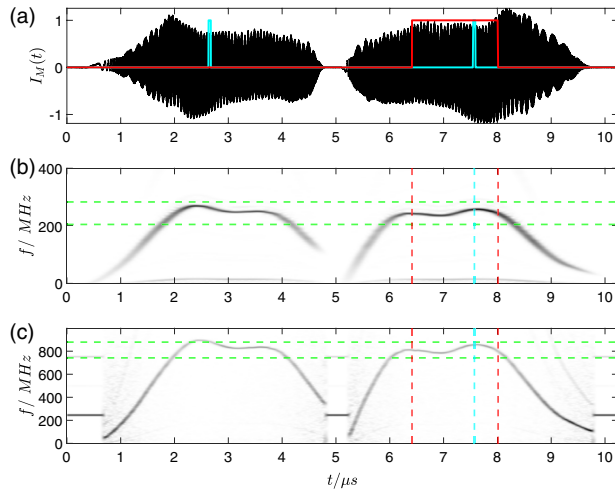


**Fig. 5.** (a) Measurement interferometer intensity signal during a single “up–down” frequency scan cycle. Blue line: FBG pulses from frequency up-scan and down-scan. Red line: time-domain window function for data analysis. (b), (c) Spectrograms for measurement and reference interferometer, respectively. Dashed lines represent timing of FBG down-scan pulse (blue); edges of time-domain window (red); edges of frequency-domain window (green).

of fringe-order identification is required. The approach is illustrated in Fig. 6, which shows expanded portions of the measurement and reference interferometer signals near the FBG pulse at two different times during the PZT ramp. The orders (denoted  $q$ ) for the fringes of the reference interferometer signals have been assigned, using the procedures described later in this section, for the plots in Figs. 6(a) and 6(c). The corresponding measurement interferometer signals [Figs. 6(b) and 6(d)] show a different phase offset with respect to the  $q = 0$  fringe that is a result of the target motion between these two frequency scans.

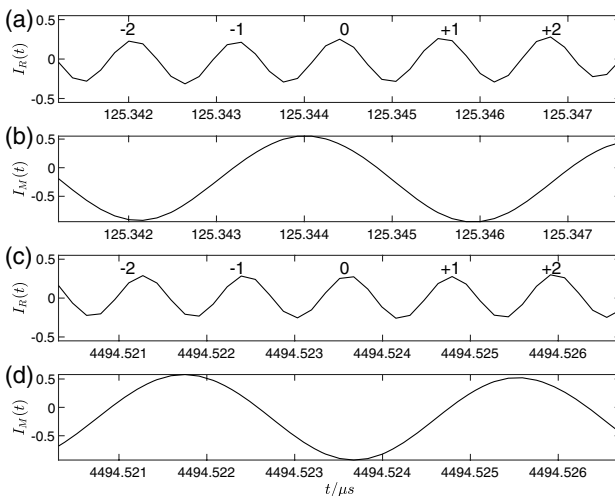


**Fig. 6.** (a) Intensity signals from reference and measurement interferometers [(a) and (b), respectively] in the neighborhood of the FBG pulse, for scan index 13 out of total 2000 scans. [PZT was  $\sim 5$  ms from peak displacement in Fig. 4(a).] (c), (d) Corresponding signals for scan index 450 (PZT close to top of the up ramp).  $-2$ ,  $-1$ ,  $0$ ,  $+1$ , and  $+2$  labels refer to the fringe order,  $q$ .

Alignment of the scans was a two-stage process. The first stage, coarse alignment, was achieved using the FBG synchronization signal that was recorded in parallel with  $I_R(t)$  and  $I_M(t)$ . The FBG pulses show some variability in shape and location from scan to scan, with a root-mean-square (rms) timing jitter of typically 1.5 sample points at the sampling rate used here. To reduce the jitter, a straight-line fit of the center of mass of the down-scan FBG pulse location versus scan index,  $s$ , was performed, and the gradient of this line defined the increment in index of the one-dimensional (1D) data vectors from one down-scan to the next. In this way, the timing jitter of one scan relative to the others was reduced to a maximum of one sample point. More precise registration was then achieved from the recovered reference interferometer phase signal, as described in Sections 4.B and 4.C.

## B. Phase Analysis

The Takeda Fourier transform method was used to extract the time-varying phase signals,  $\phi_R(t)$  and  $\phi_M(t)$ , for the reference and measurement interferometers, from the corresponding intensity signals,  $I_R(t)$  and  $I_M(t)$  [18]. This involves application of a time-domain window function, as shown in Fig. 5, to select the portion of the down-scan to be processed. The Fourier transforms of the windowed data vectors,  $\tilde{I}_R(f)$  and  $\tilde{I}_M(f)$ , were then windowed with a top hat function that is asymmetrical with respect to the frequency origin. This second window function acts as a band-pass filter, the location and width of which were chosen to let through the range of positive frequencies present in the original signals, but which block all the negative frequencies. This is illustrated in Fig. 7 for the same measurement interferometer dataset as shown in Fig. 5. Identical time-domain windows were used for all datasets; the frequency-domain windows were also the same for all of the reference interferometer signals, but varied from one measurement interferometer signal to another as the frequency content changed with the distance to the target.

The inverse Fourier transform of the windowed frequency-domain signal was then calculated, resulting in a complex

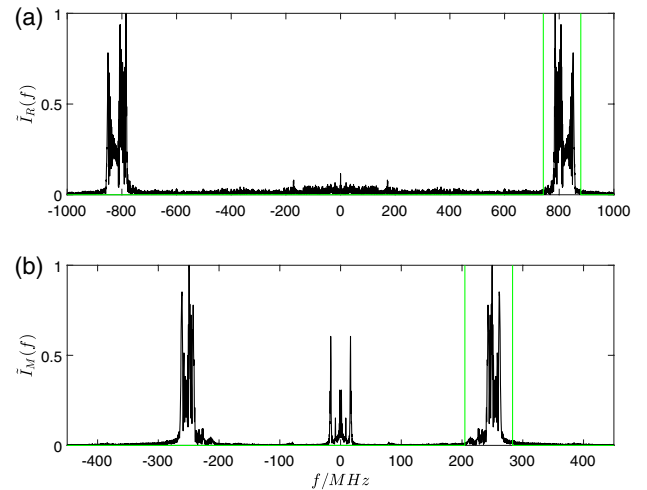


**Fig. 7.** Normalized Fourier transforms of windowed (a) reference and (b) measurement interferometer signals from a single frequency down-scan. Frequency-domain window functions are shown in green.

time-domain signal  $I'_M(t)$ . The steps above can be summarized by the following equation:

$$I'_M(t) = \mathcal{F}^{-1}\{\mathcal{W}_f(f)\mathcal{F}\{W_t(t)I_M(t)\}\}, \quad (9)$$

where  $W_f$  and  $W_t$  are the frequency and time-domain windows, respectively, and  $\mathcal{F}\{\dots\}$  and  $\mathcal{F}^{-1}\{\dots\}$  are the forward and inverse Fourier transform operators.

When selecting the window functions, the time-domain window should be as long as possible to maximize the effective frequency tuning range, and hence minimize the range resolution, whereas the frequency-domain window should be narrow to cut out as much intensity noise as possible. In terms of the spectrograms in Fig. 5, bounding boxes that are short and wide are therefore expected to give the best results, which in turn require a laser that has been optimized to provide highly linear frequency scans.

Wrapped phase values, i.e., values lying on the range of  $-\pi$  to  $+\pi$ , were calculated from  $I'_M(t)$  as

$$\hat{\phi}_M(t) = \text{atan}(\Im\{I'_M(t)\}/\Re\{I'_M(t)\}), \quad (10)$$

where  $\Re\{\dots\}$  and  $\Im\{\dots\}$  represent the real and imaginary parts, respectively. The unwrapped phase,  $\phi_M(t)$ , was then obtained from  $\hat{\phi}_M(t)$  by adding integral multiples of  $2\pi$  to the phase at each sample point so that the phase change between adjacent points always lay in the range of  $-\pi$  to  $+\pi$ . It is convenient for the next stage in the analysis if the unwrapping starts from the sample point nearest the FBG pulse. Equations equivalent to Eqs. (9) and (10) were used to find the reference interferometer phase,  $\phi_R(t)$ , from  $I_R(t)$ . The forward and inverse transforms, phase evaluation, and unwrapping were implemented in MATLAB using the `fft`, `ifft`, `atan2`, and `unwrap` functions, respectively.

### C. Scan Linearization and Fine Alignment

The fact that the laser does not maintain a constant rate of change of frequency through a given scan, as shown by the spectrograms in Fig. 5, means that linearization of the signals is required. Without linearization, the Fourier transform (see, e.g., Fig. 7) is not a well-defined narrow peak that can be used to locate the target position to a high accuracy. One approach to linearization would be to resample the measurement interferometer intensity signal before Fourier transformation. However, as intensity is a high-frequency oscillatory signal, interpolation can introduce significant numerical errors. A better way is to resample the phase signals, since over any small time interval these are close to linear functions of time.

The time values of the original equally spaced sample points will be denoted as  $t_p$  ( $p = 0, 1, 2, \dots, N_s - 1$ ).  $N_s$  is the total number of sample points in a single scan. The fringe maxima for the reference interferometer, which, as stated previously, provide the “ruler markings” to linearize the measurement interferometer phase, occur at the phase values  $\phi_R = 2q\pi$  ( $q = \dots, -2, -1, 0, 1, 2, \dots$ ).  $q$  is the fringe order; the case  $q = 0$  is taken to be the fringe closest to the FBG pulse within each scan and is termed here the “pivot” point. The times  $t'_q$ , at which  $\phi_R = 2q\pi$ , were found from the vector  $\phi_R(t_p)$  by linear interpolation using MATLAB function `interp1`.

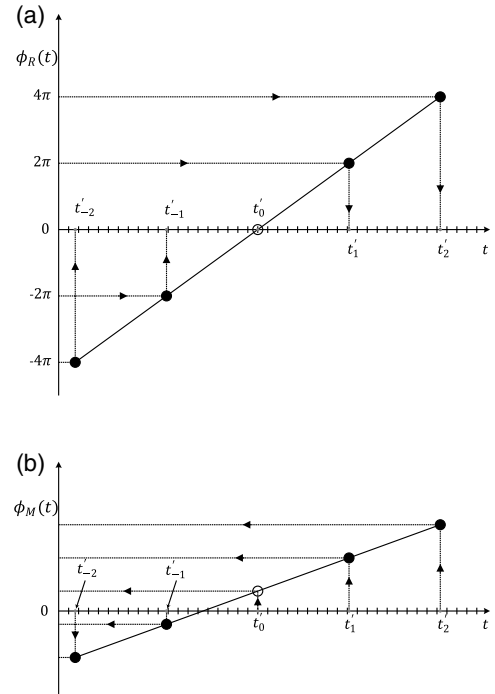


**Fig. 8.** (a) Linearization of the measurement interferometer phase,  $\phi_M(t)$ , using linearly spaced phase values  $\phi_R = 2q\pi$  ( $q = \dots, -2, -1, 0, 1, 2, \dots$ ) from the reference interferometer. (b) The corresponding time values  $t'_q$  are used to interpolate  $\phi_M(t)$ , which is sampled on the uniformly spaced time vector  $t_p$  ( $p = 0, 1, 2, \dots, N_s - 1$ ), represented by the tick marks on both horizontal axes. “Pivot point” phase values are shown as open circles.

The  $t'_q$  were then used to interpolate  $\phi_M(t_p)$ , as shown schematically in Fig. 8. The  $t'_q$  values are not, in general, equally spaced in time, so that  $\phi_M(t'_q)$  is not a linear function of time. It is, however, a linear function of variable  $q$ , provided there is no dispersion mismatch between the measurement and reference interferometers. Dispersion mismatch is clearly present in the optical setup of Fig. 3 and will produce some deviations from linearity, but this was neglected in the current study.

The procedure described above achieves, in addition to scan linearization, the required fine alignment of the measurement interferometer signal to within a small fraction of a fringe of the reference interferometer signal. There is, however, one final step required, which is to correct for a possible mis-identification of the  $q = 0$  fringe. If the FBG pulse is calculated to lie midway between two fringes, for example, the fringe selected as the pivot point may toggle between the two fringes from scan to scan. This problem was overcome by considering the points  $q = \pm 1, \pm 2$  as alternative candidate pivot points. For each candidate pivot, the phase ramp for scan  $s$ ,  $\phi_M^{(s)}(t'_q)$ , is compared with that from the previous scan,  $\phi_M^{(s-1)}(t'_q)$ . Unwrapping in the scan direction is achieved by adding an integer multiple of  $2\pi$  to  $\phi_M^{(s)}(t'_q)$  to minimize  $S$ , the sum of the squares of the differences between  $\phi_M^{(s)}(t'_q)$  and  $\phi_M^{(s-1)}(t'_q)$  ( $q = q_1, \dots, -2, -1, 0, 1, 2, \dots, q_2$ ). The candidate pivot point with the smallest  $S$  value was then taken to be the true pivot point for scan  $s$  and relabelled  $q = 0$ . In practice, the candidate pivot points with  $q = 0$  or  $\pm 1$  were always selected with this procedure.

## 5. RESULTS

The output from the previous section is a matrix of measurement interferometer phase values,  $\varphi_{s,q} = \phi_M^{(s)}(t'_q)$ : each row ( $s = 0, 1, 2, \dots, N_s - 1$ ) corresponds to an individual frequency scan, each column ( $q = q_1, q_1 + 1, \dots, q_2 - 1, q_2$ ) to an individual laser wavenumber. The phase values in the pivot point column,  $\varphi_{s,0}$ , are equivalent to those from a fixed-wavelength laser operating at the FBG wavelength,  $\lambda_{\text{FBG}} = 1310$  nm. Changes in phase relative to the starting phase,  $\Delta\varphi_{s,0} = \varphi_{s,0} - \varphi_{0,0}$ , can therefore be scaled to the axial displacement component,  $u_z$ , through the equation

$$u_z = \frac{-\lambda_{\text{FBG}} \Delta\varphi_{s,0}}{4\pi}. \quad (11)$$

The minus sign in front of the right-hand side corresponds to that given earlier in Eq. (6), but, as noted later, the required sign depends on which side of the nearest zero-OPD surface the target happened to be located. Figures 9(a) and 9(b) show  $u_z$  as it tracks the TM motion with the target in locations 7 and 9, respectively (see Table 1). For the horizontal axis, scan index  $s$  has been converted to time,  $t$ , through the known inter-scan time (9.998  $\mu\text{s}$ ). The total measured motion of just under 0.3  $\mu\text{m}$  is very close to that measured over the central 10 ms of the PZT-characterization experiment, shown previously in Fig. 4(c). Although both datasets display the expected inverted “V” shape, there is a higher level of noise in Fig. 9(a) than in Fig. 9(b). The noise can be characterized through the standard deviation of the residuals of the data with respect to a best-fit quadratic over the first 5 ms of the PZT up ramp. Values of 1.78 nm and 0.76 nm were obtained for Figs. 9(a) and 9(b), respectively.

The performance can clearly be improved upon, however, as in the above method of calculating  $u_z$ , all of the columns but one of the phase matrix  $\varphi_{s,q}$  have been discarded. One way to make use of all of the data is to fit a straight line to the phase values

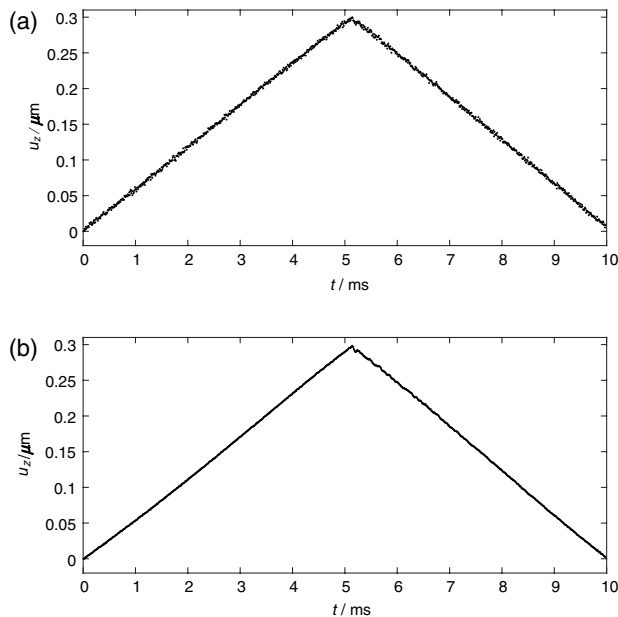


**Fig. 9.** Displacement of target mirror calculated from “pivot point” phase for target locations (a) 7 and (b) 9.

from each frequency scan, i.e., to fit (over the  $q$  variable) the equation

$$\psi_s = A_s q + B_s, \quad (12)$$

to the  $\varphi_{s,q}$  values, where  $q$  runs from  $q_1$  to  $q_2$  (−1000 to +100 in this case) in unit steps.  $B_s$  then represents an improved estimate of the phase at the pivot point. Errors can be reduced further by extracting the best-fit phase at the center of the  $q$  vector, rather than at the pivot point, as the latter is close to one end of the vector. This is easily achieved by performing the fit with respect to a vector  $q'$  that runs from  $-(q_2 - q_1)/2$  to  $(q_2 - q_1)/2$  in unit steps. The results for TM in location 9 are shown in Fig. 10(a), where the conversion from phase to displacement has been carried out using the wavelength at  $q' = 0$ , estimated as 1292.7 nm from the reference interferometer optical delay. The corresponding plot for location 7 is not shown, as, to the eye, it appears identical. The standard deviations of the residuals about the quadratic best fit curve, denoted here as  $\sigma_{u_z}$ , are reduced to 1.01 and 0.58 nm for locations 7 and 9, respectively.

As a further indication of the data quality, Fig. 10(b) shows an enlarged portion of the FSI-measured displacement near the time of maximum PZT displacement. Each point represents an independent measurement from a single-frequency scan. A small transient is visible after the PZT reverses its direction

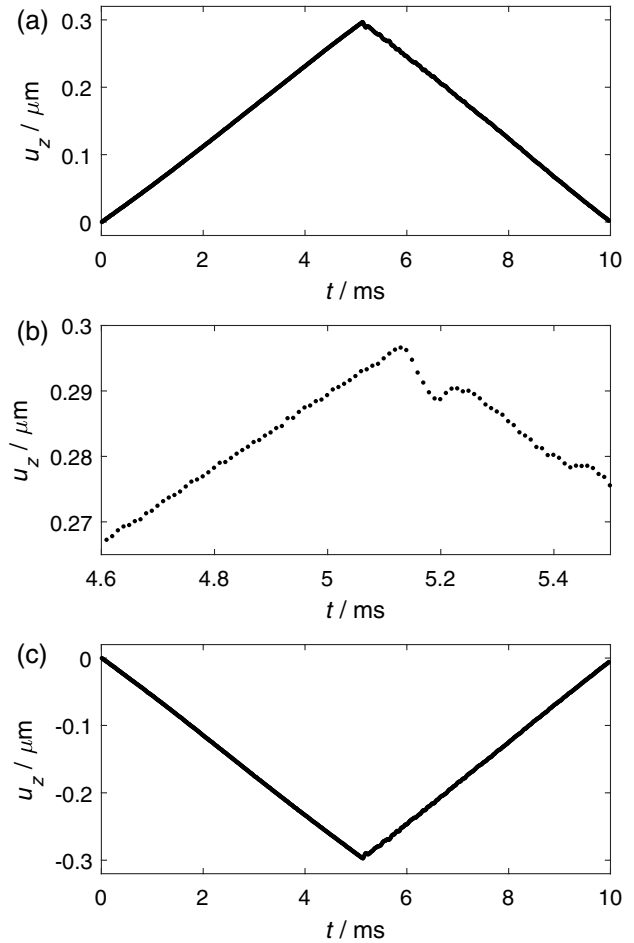


**Fig. 10.** (a) Displacement of target mirror calculated from  $B_s$  for target location 9. (b) Enlarged central portion of (a). (c) As for (a), but target in location 10.



( $t$  in the range 5.1–5.2 ms), with a frequency of around 10 kHz and initial amplitude of around 2 nm.

For datasets acquired on the other side of the zero-OPD surface, the phase change due to the PZT motion appears inverted, as shown in Fig. 10(c) for location 10. This provides a convenient way of distinguishing between positive and negative modulation frequencies in the current case, where the method described in [13] involving the use of neighboring ADL zero-OPD surfaces is not available due to the very high modulation frequencies. A more general way to distinguish between the positive and negative frequencies would be through in-phase quadrature (IQ) detection.

The gradient term  $A_s$ , estimated by fitting Eq. (12) to the phase data, is the rate of change of measurement interferometer phase per fringe-order increment of the reference interferometer. It is therefore related, as seen in Eq. (5), to the ratio of the OPDs for the measurement and reference interferometers,  $\Lambda_M$  and  $\Lambda_R$ , respectively, as follows:

$$A_s = 2\pi \Lambda_M / \Lambda_R. \quad (13)$$

$A_s$  can therefore be seen as an alternative means of measuring the target range, assuming  $\Lambda_R$  has been previously measured to sufficient accuracy, which is simpler and less prone to numerical errors than the conventional process of linearizing the intensity signal and then determining the Fourier-domain peak location.

The TM range due to the motion of the PZT, measured with TM at locations 7 and 9, is shown in Figs. 11(a) and 11(b), respectively. The  $A_s$  values have been converted to range through the scaling factor  $C = 0.285875 \text{ rad mm}^{-1}$ , as determined through the calibration experiment described later in this section. The graphs replicate the displacement of TM but are inverted because a positive axial displacement corresponds to a decrease in target range. The level of noise is significantly higher than for the displacement-time plots: the standard deviation about the best quadratic fit to the PZT up ramp,  $\sigma_z$ , is 98.6 and 18.0 nm for positions 7 and 9, respectively. The values of  $\sigma_z$  for all 12 locations are given in Table 1.

The range estimate plots in Figs. 11(a) and 11(b) contain a contribution arising from the target motion: an upwards shift as the PZT moves towards the interferometer and a downwards shift as it moves away. This can be interpreted as being due to the Doppler shift in frequency on reflection from a moving mirror, or it can be interpreted as the drift error, which is discussed further in the next section. However, the symmetrical nature of the plots about the point when the PZT reverses direction indicates that the error is so small as to be invisible, even with the lower noise level present in Fig. 11(b). Attempts to estimate target velocity from the Doppler shift, by subtracting a range value calculated from a laser down-scan from one made with an up-scan, will therefore be unsuccessful. A better way to estimate velocity is to make use of the previously calculated high-quality displacement data. Figure 11(c) shows the result of a simple centered finite difference operator, using the nearest-neighbor displacement values, on the data from Fig. 10(a). The standard deviation of the residuals about a best-fit straight line to the first 5 ms of the velocity data is  $11.7 \mu\text{m s}^{-1}$ .

Similar time histories of  $A_s$  were also calculated for the other 10 TM locations. The time-averaged value,  $\bar{A}$ , for each location

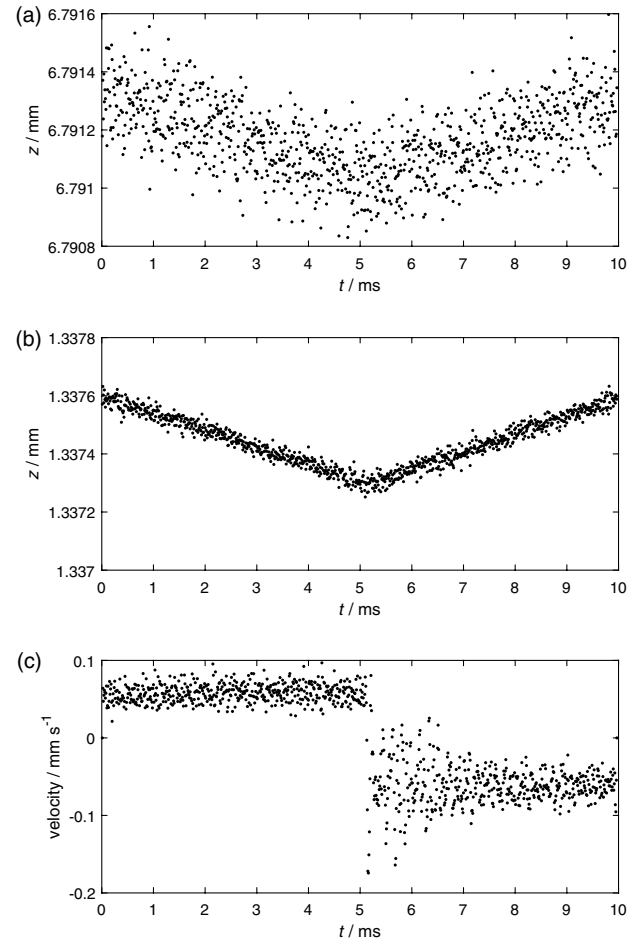


**Fig. 11.** FSI-measured range from straight-line fits to rows of matrix  $\varphi_{ij}$ , with target in location (a) 7 and (b) 9. (c) Velocity of TM calculated from the displacement data of Fig. 10(a).

and the corresponding TM range,  $z_{\text{TM}}$ , as measured by the Renishaw stabilized interferometer are listed in Table 1 and are plotted in Fig. 12. A best-fit line of the form

$$\bar{A} = C z_{\text{TM}} + D_1 \quad (010 \text{ bit configuration locations}),$$

$$\bar{A} = C z_{\text{TM}} + D_2 \quad (101 \text{ bit configuration locations}) \quad (14)$$

is shown as superimposed on the data. The three adjustable parameters in Eq. (14) are  $C$  (which equals  $4\pi/\Lambda_R$ ),  $D_1$  (the frequency at location 1 when the Renishaw interferometer was zeroed), and  $D_2$ , which differs from  $D_1$  due to the optical delay between the two bit configurations introduced by the ADL. In general, absolute distance measurement by an  $N$ -bit ADL requires  $N + 1$  unknown path lengths to be determined by a prior calibration. A process to achieve this with the Renishaw interferometer for the 3-bit ADL was described in [13]: the four unknowns were determined in a least-squares sense from the frequencies measured from all  $2^N$  bit configurations, while the target was kept in a fixed location. In the current case, only a subset of calibration constants is required, since only two bit configurations were activated. The  $D_1$  and  $D_2$  values in Eq. (14) characterize the OPDs between object and reference waves for these two bit configurations with TM located at the

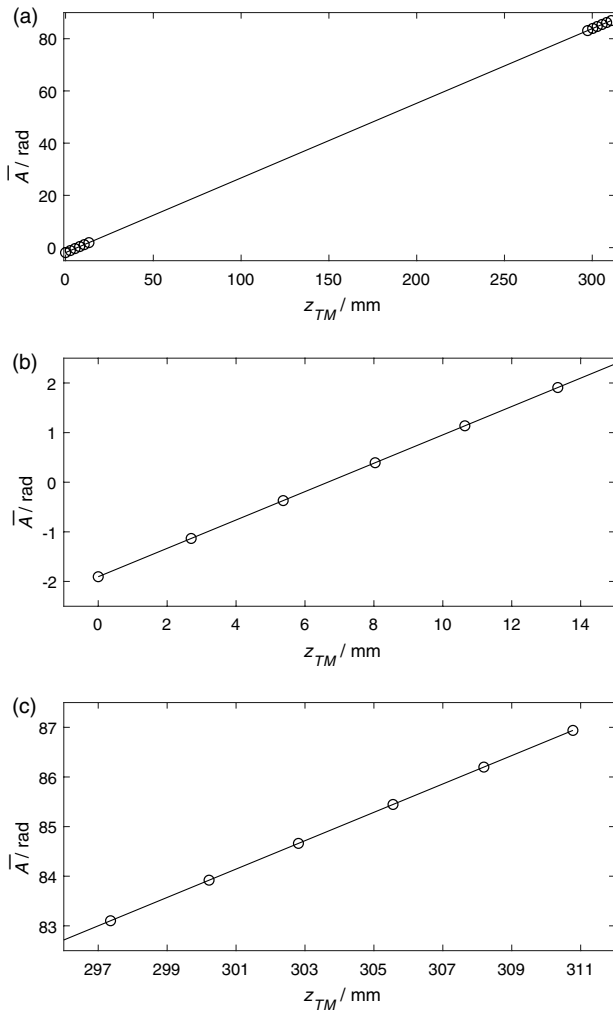


**Fig. 12.** (a) Measurement interferometer mean frequency,  $\bar{A}$ , from six locations at each of two ADL bit configurations compared to target mirror range measured by the Renishaw interferometer,  $z_{TM}$ . Continuous line: best straight-line fit to data. (b), (c) Expanded portions of (a) for bit configurations 010 and 101, respectively.  $\bar{A}$  values for the 101 bit configuration have been shifted up by 85.0439 rad.

origin of the Renishaw coordinate system. The values calculated by the least-squares analysis were  $C = 0.285875 \text{ rad mm}^{-1}$ ,  $D_1 = -1.9044 \text{ rad}$ , and  $D_2 = -86.9483 \text{ rad}$ . The  $\bar{A}$  values in Figs. 12(a) and 12(c) for the 101 bit configuration have been shifted up by  $D_1 - D_2 = 85.0439 \text{ rad}$ . The value of the reference interferometer OPD,  $\Lambda_R$ , calculated as  $4\pi/C$ , was 43.9576 mm, which may be compared to the nominal value of 44 mm, as stated in the manufacturer's datasheet. Finally, the standard deviation of the 12 residuals about the best-fit line was  $1.76 \times 10^{-4} \text{ rad}$ , which equates to a rms range error of 614 nm. For comparison, the Renishaw interferometer has a claimed accuracy of  $500 \text{ nm m}^{-1}$ . Although it might be expected that compensation for dispersion in the air would be required due to the use of a tunable source, the accuracy achieved suggests that dispersion effects can be largely mitigated through calibration with a stabilized reference interferometer operating at a single wavelength.

## 6. DISCUSSION

The sub-nanometer (nm) displacement resolution and sub-100-nm range resolution reported in the previous section, at 100 kHz sampling rates, are encouraging results. It is therefore helpful to compare the performance of this multi-functional system to existing approaches that have been optimized now over many years, but which measure range or displacement/velocity alone.

Laser Doppler vibrometers (see, for example, [19] for a recent review article) measure velocity with a single-wavelength laser and therefore cannot measure target range. Typical LDV displacement resolution, though measured on rough surfaces rather than the mirror used here, is 1–10 nm. LDV resolution can therefore be regarded as being broadly comparable to the values presented above. However, the use of a fixed-wavelength source with LDV does bring the benefit that none of the bandwidth of the photodetectors and DAQ hardware is used up for the range estimation: all is available to the vibration measurement. A carrier is normally introduced into the interference signal by means of an acousto-optic modulator, allowing vibration frequencies up to the carrier frequency [typically a few tens of megahertz (MHz)] to be accommodated. In the FSI system, this limitation is addressed to a large degree by the introduction of an ADL, which brings down the bandwidth required for the range measurement by a factor of  $2^N$ .

Although the current displacement sampling rate is 100 kHz, i.e., one velocity update per frequency scan, this could be pushed significantly higher by using the other phase values in the  $\varphi_{sq}$  matrix. Successive elements in a given row of  $\varphi_{sq}$  measure target displacement at successive time sample points, at wavenumber increments of  $2\pi/\Lambda_R$  and hence with different (but nevertheless well-defined)  $u_z/\varphi_{sq}$  scaling factors. As demonstrated in the previous section, a displacement resolution of under 2 nm is achievable with single-wavelength phase values. The ultimate limit to displacement sampling rate is the inverse of the laser fly-back time (i.e., the duration of the frequency down-scan, when no information can be recorded). For example, a  $100,000 \text{ scan s}^{-1}$  laser with an up-ramp duration of 9  $\mu\text{s}$  and down-ramp duration of 1  $\mu\text{s}$ , would allow displacement to be sampled at a uniform rate of 1 MHz and at intra-scan sampling rates limited only by the DAQ.

Turning to range measurement, nearly all previously published work has been either at much lower tuning rates or else with very narrow tuning ranges, which severely compromise range resolution. The combination of sub-100-nm range resolution over a 300-mm-deep volume at 100,000 range values  $\text{s}^{-1}$  is enabled at sub-gigahertz (GHz) bandwidth requirements through the use of an ADL. Current commercial FSI systems provide scan rates of just a few kilohertz (kHz). An immediate benefit of the 100 kHz scan rate is the reduced susceptibility to range measurement errors from moving targets. Target motion of  $\delta z$  during a frequency scan range of  $\Delta\omega$  about a center frequency  $\omega_c$  results in a range error of  $(\omega_c/\Delta\omega)\delta z$ . Previous solutions to this problem, as outlined in Section 1, have included fairly complex approaches such as the use of an LDV in parallel with the FSI system, synchronized up/down scanning lasers, four-wave mixing, etc. In the current case, the relevant target motion is the  $\sim 0.1 \text{ nm}$  that occurs during the

1.7  $\mu\text{s}$ , for which the time window is non-zero, as shown in Fig. 5. The tuning range of the laser within this window can be calculated from the  $q$  values  $q_1 = -1000$  and  $q_2 = 100$ , and the fact that each  $q$  increment corresponds to a wavenumber change of  $2\pi/\Lambda_R$ , to be 1272 nm to 1314 nm, i.e., 42 nm. The range error amplification factor ( $\omega_c/\Delta\omega$ ) is 31. The range error produced by this artefact is therefore  $\sim 3$  nm, which is insignificant compared to the random range errors of 20–100 nm. It was for this reason that the data analysis in the previous section needed only unidirectional scan data. However, for target velocities an order of magnitude or more higher, or laser scan rates an order of magnitude lower, motion artefacts would start to become significant.

The strong variation of random range errors with distance from the nearest zero-OPD surface, visible in Figs. 11(a) and 11(b) and the  $\sigma_z$  data from Table 1, deserves comment. The locations with 50, 150, and 250 MHz maximum modulation frequencies had average  $\sigma_z$  values of 21, 56, and 98 nm, respectively. This variation cannot be explained by the widths of the frequency-domain windows, which were broadly comparable at 78, 137, and 57 MHz, respectively. A more likely explanation is frequency jitter in the scans. If the instantaneous angular frequency differs from the expected value by  $\varepsilon(t)$ , then a phase error  $\varepsilon(t)\Lambda_M/c$ , i.e., proportional to distance from the relevant zero-OPD surface, will result. The analysis procedure described in the previous section will remove low-frequency errors, for example scan non-linearities, but not the high-frequency ones. The use of an ADL can therefore be seen to have the additional benefit, beyond that of reducing the maximum modulation frequency, of allowing control of the maximum range error through the measurement volume.

Selection of the ADL design parameters follows from the FSI measurement volume, defined by the minimum and maximum ranges,  $z_{\min}$  and  $z_{\max}$ , respectively. The sampling rate  $f_D$  of the chosen DAQ will determine the  $d_0$  parameter from its associated frequency  $f_0 = \frac{1}{2\pi} \frac{\Delta\omega}{\Delta t} \frac{d_0}{c} \approx d_0 f_s \frac{\Delta\lambda}{\lambda_c^2}$ . For IQ detection,  $f_D = f_0$ , while in the case of a single ABPD  $f_D = 2f_0$ . The number of switches required,  $N$ , can then be determined by Eq. (8), i.e.,  $2^N d_0 = 2(z_{\max} - z_{\min})$ . In order to make full use of the DAQ's bandwidth, the OPD of the reference interferometer,  $\Lambda_R$ , should ideally match or be comparable to  $d_0/2$ .

One final point worth making is that the dynamic range of the  $z$  measurements (i.e., maximum range/range resolution), which is often considered to be  $\sim 10^6$  for FSI, can be extended in both directions by the analysis presented here. Sub-nm range resolution could potentially be achieved from phase, i.e., either the  $\varphi_{sq}$  values or the  $B_s$  values derived from them by Eq. (12). These were unwrapped temporally in the previous section to measure displacement, but could be unwrapped instead using the  $A_s$  values to measure range, provided the phase shift on reflection from the target is known. A similar approach is used routinely in coherence scanning interferometry and has also been recently proposed in FSI [20]. Identification of the correct fringe order requires range noise below  $\lambda/4 \approx 330$  nm, a condition which is satisfied in this case as the range noise standard deviation  $\sigma_z$  is below 100 nm. At the other end, the upper limit can be increased to arbitrarily large values, as the maximum

range is doubled for each additional switch in the ADL. Coiled optical fibers could provide very long ADL delays in a suitably compact form.

## 7. CONCLUSIONS

It has been demonstrated how the combination of ADLs and a fast scanning VCSEL light source allows absolute distance, displacement, and velocity of a target to be measured over a 0.3 m range, at rates of 100,000  $\text{s}^{-1}$ , while maintaining signal modulation frequencies at sub-GHz levels. As a result, the use of low-cost DAQ hardware, and potentially real-time data processing on GPUs or FPGAs, become feasible, thus removing two significant barriers to future high-speed FSI systems. The use of phase analysis algorithms together with a separate reference interferometer have allowed a displacement resolution of under 1 nm and range resolution under 100 nm to be achieved.

**Funding.** Engineering and Physical Sciences Research Council (Future Advanced Metrology Hub, EP/P006930/1).

**Acknowledgment.** The authors wish to thank Sebastian Schaefer and colleagues at Thorlabs for the provision of a customized loan laser. Software developments by Russell Coggrave are also gratefully acknowledged.

**Disclosures.** All three authors are co-authors of a current patent application in this area.

## REFERENCES

1. M.-C. Amann, T. Bosch, M. Lescure, R. Myllylä, and M. Rioux, "Laser ranging: a critical review of usual techniques for distance measurement," *Opt. Eng.* **40**, 10–19 (2001).
2. R. Schödel, ed., *Modern Interferometry for Length Metrology* (IOP Publishing, 2018).
3. J. A. Stone, A. Stejskal, and L. Howard, "Absolute interferometry with a 670-nm external cavity diode laser," *Appl. Opt.* **38**, 5981–5994 (1999).
4. P. A. Coe, D. F. Howell, and R. B. Nickerson, "Frequency scanning interferometry in ATLAS: remote, multiple, simultaneous and precise distance measurements in a hostile environment," *Meas. Sci. Technol.* **15**, 2175–2187 (2004).
5. J. Dale, B. Hughes, A. J. Lancaster, A. J. Lewis, A. J. H. Reichold, and M. S. Warden, "Multi-channel absolute distance measurement system with sub PPM-accuracy and 20 m range using frequency scanning interferometry and gas absorption cells," *Opt. Express* **22**, 24869–24893 (2014).
6. R. Schneider, P. Thümel, and M. Stockmann, "Distance measurement of moving objects by frequency modulated laser radar," *Opt. Eng.* **40**, 33–37 (2001).
7. S. Kakuma and Y. Katase, "Frequency scanning interferometry immune to length drift using a pair of vertical-cavity surface-emitting laser diodes," *Opt. Rev.* **19**, 376–380 (2012).
8. J. J. Martinez, M. A. Campbell, M. S. Warden, E. B. Hughes, N. J. Copner, and A. J. Lewis, "Dual-sweep frequency scanning interferometry using four wave mixing," *IEEE Photon. Technol. Lett.* **27**, 733–736 (2015).
9. L. Tao, Z. Liu, W. Zhang, and Y. Zhou, "Frequency-scanning interferometry for dynamic absolute distance measurement using Kalman filter," *Opt. Lett.* **39**, 6997–7000 (2014).
10. C. Lu, G. Liu, B. Liu, F. Chen, and Y. Gan, "Absolute distance measurement system with micron-grade measurement uncertainty and

- 24 m range using frequency scanning interferometry with compensation of environmental vibration," *Opt. Express* **24**, 30215–30224 (2016).
11. T. Klein and R. Huber, "High-speed OCT light sources and systems," *Biomed. Opt. Express* **8**, 828–859 (2017).
  12. Z. Wang, B. Potsaid, L. Chen, C. Doerr, H.-C. Lee, T. Nielson, V. Jayaraman, A. E. Cable, E. Swanson, and J. G. Fujimoto, "Cubic meter volume optical coherence tomography," *Optica* **3**, 1496–1503 (2016).
  13. C. A. Pallikarakis, J. M. Huntley, and P. D. Ruiz, "Adaptive delay lines for absolute distance measurements in high-speed long-range frequency scanning interferometry," OSA Continuum (under review).
  14. A. Reichold, "Absolute distance measurement using frequency scanning interferometry," in *Modern Interferometry for Length Metrology*, R. Schödel, ed. (IOP, 2018), pp. 1–54.
  15. A. Martin, D. Dodane, L. Leviandier, D. Dolfi, A. Naughton, P. O'Brien, T. Spuessens, R. Baets, G. Lepage, P. Verheyen, P. De Heyn, P. Absil, P. Feneyrou, and J. Bourderionnet, "Photonic integrated circuit-based FMCW coherent LiDAR," *J. Lightwave Technol.* **36**, 4640–4645 (2018).
  16. N. A. Ochoa and J. M. Huntley, "Convenient method for calibrating non-linear phase modulators for use in phase shifting interferometry," *Opt. Eng.* **37**, 2501–2505 (1998).
  17. C. A. Pallikarakis, J. M. Huntley, and P. D. Ruiz, "Datasets for high-speed range and velocity measurement using frequency scanning interferometry with adaptive delay lines," 2020, <https://doi.org/10.17028/rd.lboro.13050800>.
  18. M. Takeda, H. Ina, and S. Kobayashi, "Fourier-transform method of fringe-pattern analysis for computer-based topography and interferometry," *J. Opt. Soc. Am.* **72**, 156–160 (1982).
  19. S. J. Rothberg, M. S. Allen, P. Castellini, D. Di Maio, J. J. J. Dirckx, D. J. Ewins, B. J. Halkon, P. Muyschondt, N. Paone, T. Ryan, H. Steger, E. P. Tomasini, S. Vanlanduit, and J. F. Vignola, "An international review of laser Doppler vibrometry: making light work of vibration measurement," *Opt. Laser Eng.* **99**, 11–22 (2017).
  20. S. Kakuma, "Frequency scanning interferometry with nanometer precision using a vertical-cavity surface-emitting laser diode under scanning speed control," *Opt. Rev.* **22**, 869–874 (2015).